Annals of Biomedical Engineering, Vol. 34, No. 4, April 2006 *(© 2006)* pp. 575–592
DOI: 10.1007/s10439-005-9074-4

Blood Flow in Compliant Arteries: An Effective Viscoelastic Reduced Model, Numerics, and Experimental Validation

SUNČICA ČANIĆ,[1] CRAIG J. HARTLEY,[2] DOREEN ROSENSTRAUCH,[3] JOSIP TAMBAČA,[4] GIOVANNA GUIDOBONI,[1] and ANDRO MIKELIĆ[5]

[1]Department of Mathematics, University of Houston, Houston TX, 77204-3008; [2]Sections of Cardiovascular Sciences, Department of Medicine, Baylor College of Medicine, Houston, TX 77030; [3]Texas Heart Institute and the University of Texas Health Science Center at Houston, TX, 77204; [4]Department of Mathematics, University of Zagreb, Bijenička 30, Croatia; and [5]Department of Mathematics, Université Claude Bernard Lyon 1, 69622, Villeurbanne Cedex, France

(Received 31 August 2005; accepted 22 December 2005; published online: 21 March 2006)

Abstract—The focus of this work is on modeling blood flow in medium-to-large systemic arteries assuming cylindrical geometry, axially symmetric flow, and viscoelasticity of arterial walls. The aim was to develop a reduced model that would capture certain physical phenomena that have been neglected in the derivation of the standard axially symmetric one-dimensional models, while at the same time keeping the numerical simulations fast and simple, utilizing one-dimensional algorithms. The viscous Navier–Stokes equations were used to describe the flow and the linearly viscoelastic membrane equations to model the mechanical properties of arterial walls. Using asymptotic and homogenization theory, a novel closed, "one-and-a-half dimensional" model was obtained. In contrast with the standard one-dimensional model, the new model captures: (1) the viscous dissipation of the fluid, (2) the viscoelastic nature of the blood flow – vessel wall interaction, (3) the hysteresis loop in the viscoelastic arterial walls dynamics, and (4) two-dimensional flow effects to the leading-order accuracy. A numerical solver based on the 1D-Finite Element Method was developed and the numerical simulations were compared with the ultrasound imaging and Doppler flow loop measurements. Less than 3% of difference in the velocity and less than 1% of difference in the maximum diameter was detected, showing excellent agreement between the model and the experiment.

Keywords—Blood flow modeling, Viscoelasticity of arterial walls, Fluidstructure interaction.

INTRODUCTION

Local hemodynamics and temporal wall shear stress gradient are thought to be important factors in triggering the onset of focal atherogenesis leading to various complications in the cardiovascular function. Elevated temporal shear stress gradient, for example, has been shown to stimulate endothelial cell proliferation,[16] which is a precursor for graft limb thrombosis in bifurcated endografts used in endovascular treatment of aortic abdominal aneurysm. Many clinical treatments can only be studied in detail if a reliable model describing the response of the arterial wall to the pulsatile blood flow is considered.

Due to the immense complexity of the cardiovascular system, studying the interaction between blood flow and vessel walls is exceedingly difficult. Whenever possible, simplifying assumptions such as, for example, axial symmetry of endovascular prostheses and size of a considered artery, need to be taken into account.

In this vein, this work focuses on modeling blood flow in medium-to-large compliant arteries. The main interest was in modeling arterial sections that can be approximated by the cylindrical geometry allowing axially symmetric flows. The viscous incompressible Navier–Stokes equations were used to model the flow, and the linearly viscoelastic membrane equations to model the mechanical properties of the wall. The aim was to develop a fluid–structure interaction model that captures certain important physical phenomena that have been either neglected or oversimplified in the derivation of the standard one-dimensional models such as: the viscous dissipation of the fluid, the viscoelasticity of vessel walls, and the wall shear stress. At the same time, a goal was to keep the complexity of the numerical algorithm equivalent to those of one-dimensional solvers.

One-dimensional models have been studied by many authors. The first comprehensive study showing the derivation of the one-dimensional model was presented in.[3]For a detailed analysis of the model equations see, for example, Refs.[7,14] The one-dimensional model is obtained by averaging the three-dimensional incompressible Navier–Stokes equations over the cross-section of the vessel. In this process of dimension reduction a typical question of "closure" needs to be resolved. More precisely, averaging over the cross-section of the vessel does not lead to a well-posed problem unless extra information is provided. An *ad hoc* assumption in the form of an axial velocity profile is used to resolve this issue. Giving the form of the velocity profile

Address correspondence to Sunčica Čanić, Department of Mathematics, University of Houston, Houston, TX, 77204-3008. Electronic mail: canic@math.uh.edu

a priori, instead of recovering it from the solution of the problem, leads to the loss of accuracy in the quantities that are sensitive to the form of the velocity profile such as, for example, the wall shear stress.

In this work a *closed*, "one-and-a-half dimensional model" is obtained using techniques based on the asymptotic and homogenization theory for porous media flows. The equations are closed in the sense that the axial velocity profile is calculated as one of the components of the solution to the problem. Thus, the axial velocity profile, as all the other components of the solution, depends on the data (the inlet and outlet pressure and vessel wall properties). As a result, the solution to the obtained closed model predicts the flow, the wall shear stress, and wall dynamics with a higher accuracy than the one-dimensional models.

In addition, the "one-and-a-half dimensional model" proposed in this work keeps the viscous dissipation of the fluid to the leading order. This is, again, in contrast with the one-dimensional models, where the effects of fluid viscosity are encountered as a sink in the axial momentum, oversimplifying the smoothing properties of the fluid viscosity in terms of a viscous drag force.

Perhaps the most interesting feature of the model studied in this work is its simple form which is capable of *explicitly* capturing two distinct phenomena that contribute to the viscoelastic behavior of vessel walls. One is the influence of fluid viscosity on the vessel wall dynamics, and a separate one is the vessel walls viscoelastic mechanical properties. The viscoelastic mechanical properties of vessel walls were modeled by utilizing a simple viscoelastic membrane model (2.3) which is based on the Kelvin–Voigt viscoelasticity (2.2). Our numerical simulations reveal the hysteresis behavior in the pressure–diameter diagram observed in the measurements reported in Refs.[1,2,4] In contrast, we show that fluid viscosity does not, to the leading order, effect the hysteresis behavior of vessel walls. Rather, we found that the viscous fluid imparts long-term memory effects on the dynamics of the vessel walls (see the section on "Viscoelasticity of the Fluid–Structure Interaction").

Understanding particular viscoelastic contributions to the vessel wall dynamics is important, among other things, in the measurements of the mechanical properties of vessel walls. If the measurements are performed *in vivo*, the contributions of the viscous fluid need to be factored out before quantifying the mechanical, viscoelastic properties of the arterial walls.

A numerical algorithm based on the one-dimensional Finite Element Method (FEM) was developed for the numerical calculation of the solution to the fluid–structure interaction problem. The results of the numerical simulations were compared with experimental measurements. A mock circulatory pulsatile flow loop with (compliant) latex tubing was assembled at the Research Laboratory at the Texas Heart Institute. Ultrasound measurements and Doppler methods were used to detect the wall behavior and fluid velocity. Nondairy coffee creamer was dispersed in water to enable ultrasound measurements of the fluid velocity. Excellent agreement between the numerically calculated and experimentally measured quantities was obtained.

DESCRIPTION OF THE PROBLEM

This work focuses on the study of blood flow in major systemic arteries such as the aorta or iliac arteries. A typical vessel is modeled as an axisymmetric compliant cylinder.

Using Ω to denote cylinder's reference state, assumed at the reference pressure p_{ref}, in cylindrical coordinates (r, z, θ) domain Ω is defined by

$$\Omega = \{x = (r\cos\theta, r\sin\theta, z) \in \mathbb{R}^3 : r \in (0, R(z)), \\ \theta \in (0, 2\pi), z \in (0, L)\} .$$

Here z is the axis of symmetry of the cylinder, L is its length, $R(z)$ is the reference radius, and r and θ are the polar coordinates describing each cross-section of the cylinder. The reference radius $R(z)$ can vary along the cylinder's length to describe vessel tapering, mild stenoses or aneurysms. In typical systemic arteries the aspect ratio, defined by

$$\varepsilon = \frac{R_{\max}}{L}, \tag{2.1}$$

is small, namely $\varepsilon \ll 1$. In this work, a system of equations will be derived approximating the flow to the ϵ^2-accuracy.

The reference cylinder Ω has the lateral boundary, Σ, see Fig. 1, that represents the vessel wall at reference pressure p_{ref}:

$$\Sigma = \{x = (R(z)\cos\theta, R(z)\sin\theta, z) \in \mathbb{R}^3 : \theta \in (0, 2\pi), \\ z \in (0, L)\} .$$

It is assumed that the *in vivo* arteries are prestretched under internal pressure load, that the arterial walls are longitudinally tethered, and that they undergo radial motions only. The linearly viscoelastic membrane model is used to describe the wall behavior. More precisely, it is assumed that the wall behaves as a homogeneous, isotropic, linearly viscoelastic membrane with thickness h, radial displacement $\eta(z, t)$, and "Kelvin–Voigt" viscoelasticity in the radial direction. The Kelvin–Voigt viscoelasticity for a three-dimensional isotropic and homogeneous body relates the total stress tensor, described by the coefficients t_{kl}, to the infinitesimal strains e_{kl} and the time-derivative of the strains $\partial_t e_{kl}$ through the following relationship[13]

$$t_{kl} = (\lambda_e + \lambda_v\partial_t)I_e\delta_{kl} + 2(\mu_e + \mu_v\partial_t)e_{kl}, \\ k, l = 1, 2, 3 , \tag{2.2}$$

where λ_e and μ_e are the Lamé constants of elasticity, λ_v and μ_v are their corresponding viscoelastic counterparts, δ_{kl} is the Kronecker delta, and $I_e := \Sigma_{i=1}^3 e_{ii}$.

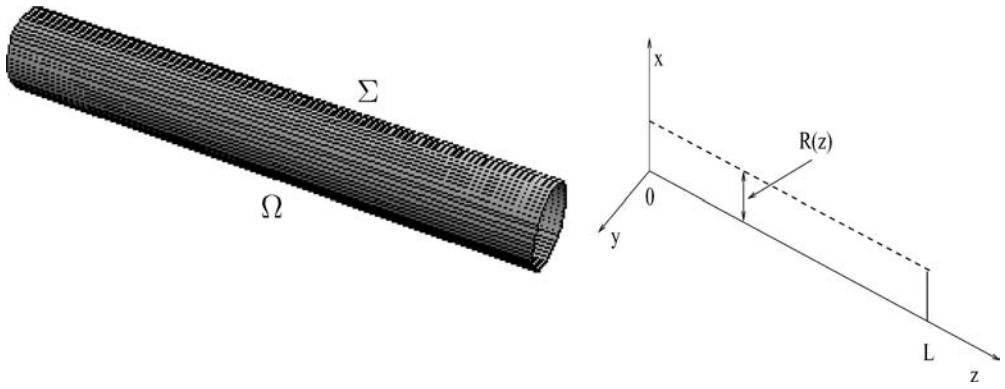

FIGURE 1. The reference domain Ω.

The motion of the wall is described by the second Newton's law of motion relating the force with wall acceleration, wall velocity, and wall displacement. Assuming external transverse (radial) loading and zero longitudinal displacement, the second Newton's law of motion reads[6]

$$f_{\mathrm{r}} = h\rho_{\mathrm{w}}\frac{\partial^2\eta}{\partial t^2} + \frac{Eh}{1-\sigma^2}\frac{1}{R^2}\eta + p_{\mathrm{ref}}\frac{\eta}{R} + \frac{hC_{\mathrm{v}}}{R^2}\frac{\partial\eta}{\partial t}. \quad (2.3)$$

Here, f_{r} describes the radial component of the external force acting on the thin shell, ρ_{w} is the wall density, E is the Youngs modulus of elasticity, σ is the Poisson ratio, and C_{v} is the viscosity constant. The following relationship holds between the parameters in (2.3) and the Lamé constants:

$$\frac{E}{1-\sigma^2} = \frac{2\mu\lambda}{\lambda+2\mu} + 2\mu, \quad C_{\mathrm{v}} = \frac{2\mu_{\mathrm{v}}\lambda_{\mathrm{v}}}{\lambda_{\mathrm{v}}+2\mu_{\mathrm{v}}} + 2\mu_{\mathrm{v}}\,.$$

Equation (2.3) says that the external force f_{r} is counterbalanced by the total force of the wall which is a resultant of the following three contributions: (1) the rate of change of momentum, *i.e.* wall acceleration described by the first term on the right-hand side, (2) the total internal stress caused by the wall stretching described by the second and third terms on the right-hand side, and (3) viscous dissipation effecting the velocity of the wall motion, described by the last term in (2.3). Equation (2.3) describes dynamic equilibrium for which the sum of total forces must equal zero.

The deformed cylinder at time t, whose radius includes the displacement $\eta(z,t)$ from the reference configuration, see Fig. 2, will be denoted by $\Omega(t)$

$$\Omega(t) = \{(r\cos\theta, r\sin\theta, z) \in \mathbb{R}^3 : r \in (0, R(z)+\eta(t,z)), \\ \theta \in (0, 2\pi), z \in (0, L)\}\,,$$

while the wall of the cylinder at time t is denoted by

$$\Sigma(t) = \{((R(z)+\eta(t,z))\cos\theta, (R(z) \\ + \eta(t,z))\sin\theta, z) \in \mathbb{R}^3 : \theta \in (0,2\pi), z \in (0,L)\}.$$

The flow of blood in medium-to-large systemic arteries is described by the Navier–Stokes equations for an incompressible, viscous, Newtonian fluid.[19] Assuming axially symmetric flow, the radial and axial component of the fluid velocity $\boldsymbol{v}(r,z,t) = (v_r(r,z,t), v_z(r,z,t))$ and pressure $p(r,z,t)$ satisfy the balance of radial and axial momentum and conservation of mass, given by the Navier–Stokes

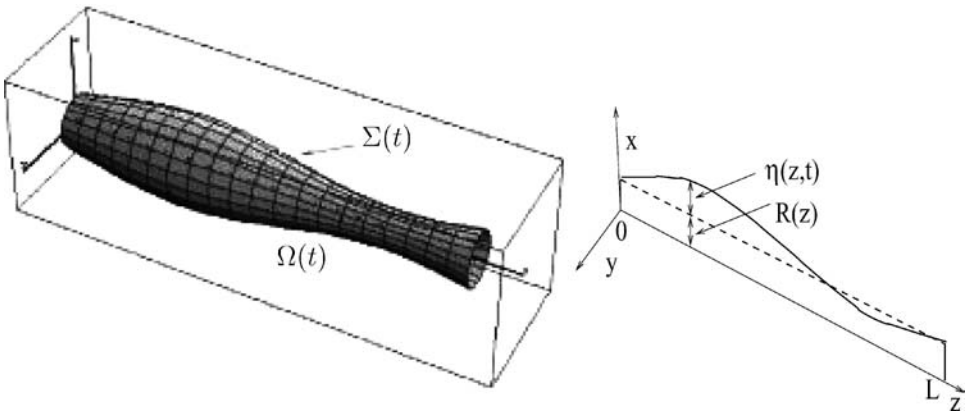

FIGURE 2. The domain Ω(*t*).

equations in cylindrical coordinates:

$$\rho_F\left(\frac{\partial v_r}{\partial t}+v_r\frac{\partial v_r}{\partial r}+v_z\frac{\partial v_r}{\partial z}\right)+\frac{\partial p}{\partial r}$$
$$=\mu\left(\frac{\partial^2 v_r}{\partial r^2}+\frac{\partial^2 v_r}{\partial z^2}+\frac{1}{r}\frac{\partial v_r}{\partial r}-\frac{v_r}{r^2}\right) \quad (2.4)$$

$$\rho_F\left(\frac{\partial v_z}{\partial t}+v_r\frac{\partial v_z}{\partial r}+v_z\frac{\partial v_z}{\partial z}\right)+\frac{\partial p}{\partial z}$$
$$=\mu\left(\frac{\partial^2 v_z}{\partial r^2}+\frac{\partial^2 v_z}{\partial z^2}+\frac{1}{r}\frac{\partial v_z}{\partial r}\right) \quad (2.5)$$

$$\frac{\partial v_r}{\partial r}+\frac{\partial v_z}{\partial z}+\frac{v_r}{r}=0. \quad (2.6)$$

Here μ is the fluid dynamic viscosity coefficient and ρ_{F} is the fluid density. The three terms on the left of the first two equations, multiplying ρ_{F}, describe fluid inertia. The other terms describe the sum of all forces acting on the fluid. The last equation describing conservation of mass is derived by postulating that mass can neither be created nor destroyed. It is also known as the incompressibility condition. These equations describe how fluid velocity and pressure change, subject to certain initial and boundary conditions. The following inlet and outlet boundary data lead to a well-defined problem:

- **Inlet data** ($z=0$):
  - (i) $p+\rho_{\mathrm{F}}(v_z)^2/2=P_0(t)+p_{\mathrm{ref}}$ (the dynamic pressure is prescribed),
  - (ii) $v_r=0$ (fluid is entering the tube parallel to the axis of symmetry)
  - (iii) $\eta=0$ (zero displacement at the inlet; in the reduced model, see the section on "The One-and-a-Half-Dimensional Reduced Model," the zero displacement condition is relaxed; this is typical for reduced models where the boundary layer phenomena near the edges with high stress concentrations are lost)
- **Outlet data** ($z=L$):
  - (i) $p+\rho_{\mathrm{F}}(v_z)^2/2=P_L(t)+p_{\mathrm{ref}}$ (same as at the inlet),
  - (ii) $v_r=0$ (same as at the inlet),
  - (iii) $\eta=0$ (same as at the inlet).

Initially the fluid is assumed to be at rest, with zero displacement from the reference cylinder:

- **Initial data:** $\eta=\frac{\partial\eta}{\partial t}=0, v=0.$

  This set of initial and boundary data gives rise to a well-posed problem which can be solved numerically.

The cylinder's lateral boundary $\Sigma(t)$ pulsates in time as blood flows through the cylinder. The fluid flows through the cylinder due to the pressure gradient between the inlet and the outlet, and due to the forces exerted by the cylinder's elastic/viscoelastic wall. More precisely, as the left ventricle contracts and expels blood into the aorta, it imparts kinetic energy to the blood, which stretches the aorta as aortic pressure reaches its systolic peak. In diastole the walls of the aorta recoil, releasing the potential energy stored during systole. This maintains adequate pressure on the reducing blood volume and keeps the flow moving forward. This interaction between blood flow and elastic/viscoelastic wall, known in the mathematical literature as the fluid–structure interaction, is described by two conditions:

- The no-slip condition describes the fact that the particles of the fluid stick to the wall. They move with the same velocity as the vessel wall itself:

  $$v_r(R+\eta(z,t),z,t)=\frac{\partial\eta(z,t)}{\partial t},$$
  $$v_z(R+\eta(z,t),z,t)=0. \quad (2.7)$$

  Notice that only the radial component of the vessel wall velocity is nonzero since only the radial component of the displacement is assumed to be non-zero.
- Balance of forces states that the contact force acting by the wall to the fluid is counter-balanced by the contact force acting by the fluid to the wall:

  $$f_{\mathrm{r}}=[(p-p_{\mathrm{ref}})\mathbf{I}-2\mu D(\boldsymbol{v})]\boldsymbol{n}\cdot\boldsymbol{e}_{\mathrm{r}}\left(1+\frac{\eta}{R}\right)$$
  $$\times\sqrt{1+(\partial_z\eta)^2}\,, \quad (2.8)$$

  where f_{r} is given by the viscoelastic membrane equation (2.3) and the right-hand side of (2.8) describes the contact force of the fluid. Here $D(\boldsymbol{v})$ is the rate-of-strain tensor or the symmetrized gradient of the velocity, $\boldsymbol{n}$ is the vector normal to the deformed boundary $\Sigma(t)$, and $\boldsymbol{e}_{\mathrm{r}}$ is the radial unit vector.

These two conditions are evaluated at the lateral boundary $\Sigma(t)$.

Thus, the problem of finding the axially symmetric flow of an incompressible, viscous fluid through a cylindrical domain with a compliant wall consists of solving the fluid equations (2.4)–(2.6) in the cylindrical domain $\Omega(t)$, with the initial conditions and the inlet and outlet boundary data specified above, and with the lateral boundary conditions described by (2.7) and (2.8). This is a difficult problem from both the numerical and mathematical point of view. The main difficulties lie in the fact that the fluid equations are nonlinear due to the quadratic convection terms in equations (2.4) and (2.5) (those are the second and third term describing convection by the fluid with velocity $\boldsymbol{v}$ which is

not known *a priori*), and that the shape of the domain $\Omega(t)$ is not known *a priori*, but depends on the solution as well. Real-time simulations of this problem are still unfeasible. Whenever possible, simplified models are called for. In this work a simplified, effective, model is derived, holding for small aspect ratios ϵ, namely, for the aspect ratios and flow conditions that are typical for the abdominal aorta or iliac arteries.

THE REDUCED MODEL EQUATIONS

Using asymptotic analysis coupled with the ideas from homogenization theory of porous media flows, a set of reduced, simplified equations was obtained. The derivation of the equations is not described in detail. Rather, the reader should consult Refs.[8–11,24] for the details of the analysis. To simplify matters, the nondimensional analysis described below is given for a constant reference radius R. The final equations in dimensional form, presented in the section on "The One-and-a-Half Dimensional Reduced Model," hold for a nonconstant, slowly varying radius $R = R(z)$. A novelty here is including viscosity in the wall model, which was not considered in Refs.[8–11,24] The main steps in the derivation of the reduced model equations can be summarized as follows.

The Two-Dimensional Reduced Equations

To detect the small terms in the underlying problem it is a custom to write the model equations in nondimensional form. For that purpose the nondimensional independent variables $\tilde{r}$, $\tilde{z}$ and $\tilde{t}$ are introduced via

$$r = R\tilde{r}, \quad z = L\tilde{z}, \quad t = \frac{1}{\omega}\tilde{t},$$

where

$$\omega = \frac{1}{L}\sqrt{\frac{1}{\rho_{\mathrm{F}}}\left(\frac{hE}{R(1-\sigma^2)} + p_{\mathrm{ref}}\right)}. \tag{3.9}$$

The time scale $1/\omega$ is determined by the frequency of oscillations of the vessel wall caused by the pressure wave in the fluid. The units describing ω are $1/s$. The form of ω is obtained in Ref.[10] from an energy estimate.

Next, the nondimensional velocity $\tilde{\boldsymbol{v}}$, displacement $\tilde{\eta}$ and pressure $\tilde{p}$ are introduced via $\boldsymbol{v} = V\tilde{\boldsymbol{v}}$, $\eta = \Xi\tilde{\eta}$ and $p = \rho_{\mathrm{F}}V^2\tilde{p}$. Expanding the unknown functions $\tilde{\eta}$, $\tilde{\boldsymbol{v}}$, and $\tilde{p}$ in terms of the small parameter ϵ gives

$$\boldsymbol{v} = V\{\tilde{\boldsymbol{v}}^0 + \varepsilon\tilde{\boldsymbol{v}}^1 + \cdots\},$$

where

$$2V = \frac{\mathcal{P}}{\sqrt{\rho_{\mathrm{F}}}}\left(\frac{hE}{R(1-\sigma^2)} + p_{\mathrm{ref}}\right)^{-\frac{1}{2}} \tag{3.10}$$

$$\eta = \Xi\{\tilde{\eta}^0 + \varepsilon\tilde{\eta}^1 + \cdots\},$$

where

$$2\Xi = \mathcal{P}R\left(\frac{hE}{R(1-\sigma^2)} + p_{\mathrm{ref}}\right)^{-1}, \tag{3.11}$$

$$p = \rho_{\mathrm{F}}V^2\{\tilde{p}^0 + \varepsilon\tilde{p}^1 + \cdots\}. \tag{3.12}$$

Here, the leading-order coefficients V and Ξ measure the magnitude of the velocity and the displacement in terms of the parameters of the problem. They were calculated from the *a priori* solution estimates, presented in Ref.[9] Letter $\mathcal{P}$ denotes a norm that measures the magnitude of the inlet and outlet pressure, the pressure drop, and the averaged pressure in one cardiac cycle: $\mathcal{P}^2 := \sup_{z,t}|\hat{p}|^2 + (\sup_z \int_0^t |\hat{p}_t|d\tau)^2 + T\int_0^t |P_L(\tau) - P_0(\tau)|^2 d\tau$, where $\hat{p}(t) = \frac{P_L(t)-P_0(t)}{L}z + P_0(t)$.

Following standard ideas in asymptotic theory these expansions are substituted in the original equations. The terms of order ϵ^2 and smaller are neglected giving rise to the following ϵ^2 approximations[9]:

- The ε^2-approximation of the balance of radial momentum is $\partial\tilde{p}/\partial\tilde{r} = 0$. This implies that the ϵ^2-approximation of the problem considered here is a hydrostatic one, namely, that the pressure $\tilde{p} = \tilde{p}^0 + \varepsilon\tilde{p}^1$ is constant across the cross-section of the tube. Thus $\tilde{p} = \tilde{p}(\tilde{z}, \tilde{t})$
- The leading order approximation of the radial component of the velocity, $\tilde{v}_r^0$, is zero. Namely, $v_r = V(\epsilon\tilde{v}_r^1 + \ldots)$ while $v_z = V(\tilde{v}_z^0 + \epsilon\tilde{v}_z^1 + \ldots)$, which says that the radial component of the velocity is smaller than the axial component of the velocity by a factor of ϵ. This follows from the leading-order terms in the conservation of mass equation.[9]
- The ε^2-approximation of the contact condition (2.8), derived in Ref.[9] shows that the fluid pressure term in (2.8) is the only term that affects the motion of the lateral boundary to the leading order. More precisely, the ε^2-approximation of (2.8) in nondimensional variables reads:

$$\tilde{p} - \tilde{p}_{\mathrm{ref}} = \frac{1}{\rho_{\mathrm{F}}V^2}\left\{\left(\frac{Eh}{(1-\sigma^2)R} + p_{\mathrm{ref}}\right)\frac{\Xi}{R}\tilde{\eta} + \frac{h}{R}C_{\mathrm{v}}\omega\frac{\Xi}{R}\frac{\partial\tilde{\eta}}{\partial\tilde{t}}\right\}. \tag{3.13}$$

- The following two-dimensional initial-boundary value problem, defined on the scaled domain $\tilde{r} \in (0,1)$, $\tilde{z} \in (0,1)$, $\tilde{t} > 0$, describes an ε^2 approximation of the fluid–structure interaction problem:
  The fluid equations:

$$\mathrm{Sh}\frac{\partial\tilde{v}_z}{\partial\tilde{t}} + \tilde{v}_z\frac{\partial\tilde{v}_z}{\partial\tilde{z}} + \tilde{v}_r\frac{\partial\tilde{v}_z}{\partial\tilde{r}} + \frac{\partial\tilde{p}}{\partial\tilde{z}} = \frac{1}{Re}\left\{\frac{1}{\tilde{r}}\frac{\partial}{\partial\tilde{r}}\left(\tilde{r}\frac{\partial\tilde{v}_z}{\partial\tilde{r}}\right)\right\}, \tag{3.14}$$

$$\frac{\partial}{\partial \tilde{r}}(\tilde{r}\tilde{v}_r) + \frac{\partial}{\partial \tilde{z}}(\tilde{r}\tilde{v}_z) = 0, \tag{3.15}$$

$$\frac{\partial \tilde{p}}{\partial \tilde{r}} = 0. \tag{3.16}$$

Lateral Boundary Conditions:

$$\left\{ \begin{array}{l} \text{Equation (3.13)} \\ (\tilde{v}_r, \tilde{v}_z)|_{(1,\tilde{z},t)} = \left(\frac{\partial \tilde{\eta}}{\partial \tilde{t}}|_{(\tilde{z},\tilde{t})}, 0\right) \end{array} \right\} \quad \text{for } \tilde{z} \in (0,1), \quad \tilde{t} > 0. \tag{3.16}$$

Inlet/Outlet Boundary Data:

$$\left\{ \begin{array}{l} \tilde{\eta}|_{(z=0/L,\tilde{t})} = 0,\ \tilde{p}|_{(z=0/L,\tilde{t})} = \frac{(P_{0/L}(\tilde{t}) + p_{\text{ref}})}{\rho_{\text{F}} V^2}, \\ \text{with } \tilde{p} \text{ given by (3.13)}, \\ \tilde{v}_{\tilde{r}}|_{(1,z=0/L,\tilde{t})} = 0 \end{array} \right\}$$

Initial Data:

$$\tilde{\boldsymbol{v}}|_{(\tilde{r},\tilde{z},0)} = 0,\ \tilde{\eta}|_{(\tilde{z},0)} = 0.$$

Here $\tilde{v}_r : \tilde{v}_r^1 + \varepsilon \tilde{v}_r^2$ so that $v_r^\varepsilon = \varepsilon V(\tilde{v}_r + \mathcal{O}(\varepsilon^2))$, $\tilde{v}_z := \tilde{v}_z^0 + \varepsilon \tilde{v}_z^1$ so that $v_z^\varepsilon = V(\tilde{v}_z + \mathcal{O}(\varepsilon^2))$, $\tilde{p} := \tilde{p}^0 + \varepsilon \tilde{p}^1$ so that $p^\varepsilon = \rho_F V^2(\tilde{p} + \mathcal{O}(\varepsilon^2))$ and $\tilde{\eta} := \tilde{\eta}^0 + \varepsilon \tilde{\eta}^1$ so that $\eta^\varepsilon = \Xi(\tilde{\eta} + \mathcal{O}(\varepsilon^2))$. The Stronuhal and the Reynolds numbers are given by

$$Sh = \frac{L\omega}{V} \quad \text{and} \quad Re = \frac{\rho_{\text{F}} V R^2}{\mu L}. \tag{3.17}$$

In dimensional variables the pressure equation (3.13) with $C_{\text{v}} = 0$ reads

$$p(z,t) - p_{\text{ref}} = \left(\frac{hE}{R(1-\sigma^2)} + p_{\text{ref}}\right)\frac{\eta(z,t)}{R}, \tag{3.18}$$

which is known as the Law of Laplace, typically used in literature to model the vessel wall behavior in one-dimensional blood flow models.[7,15,20] Here, the p_{ref} term on the right-hand side takes into account the fact that arteries *in vivo* are prestressed and that η measures the displacement from the prestressed radius R. Furthermore, notice that the ε^2-approximation of the inlet and outlet boundary conditions consists of prescribing only the pressure and not the dynamic pressure.

This two-dimensional reduced problem is still rather complex to solve numerically because of the nonlinearity in the fluid equations and because the equations are defined on the domain $\Omega(t)$ that is bounded by a moving boundary whose location depends on the solution. To simplify this problem even further, a typical approach in literature is to average the fluid equations across the cross-section and obtain a one-dimensional model. The resulting model is summarized next.

The One-Dimensional Model

After integrating equations (3.14)–(3.15) across the cross-section, the following system is obtained

$$\frac{\partial \tilde{A}}{\partial \tilde{t}} + \frac{\Xi}{R}\frac{\partial \tilde{m}}{\partial \tilde{z}} = 0\,, \tag{3.19}$$

$$Sh\frac{\partial \tilde{m}}{\partial \tilde{t}} + \frac{\partial}{\partial \tilde{z}}\left(\tilde{\alpha}\frac{\tilde{m}^2}{\tilde{A}}\right) + \tilde{A}\frac{\partial \tilde{p}}{\partial \tilde{z}} = \frac{2}{Re}\sqrt{\tilde{A}}\left[\frac{\partial \tilde{v}_z}{\partial \tilde{r}}\right]_{\tilde{\Sigma}}. \tag{3.20}$$

Here $\tilde{A} = (1 + \frac{\Xi}{R}\tilde{\eta})^2$ is the (scaled) cross-sectional area, $\tilde{m} = \tilde{A}\tilde{U}$ is the flow rate, $\tilde{U} = \frac{2}{\tilde{A}}\int_0^{1+\frac{\Xi}{R}\tilde{\eta}} \tilde{v}_z \tilde{r} d\tilde{r}$ is the average cross-sectional fluid velocity and $\tilde{\alpha} = \frac{2}{\tilde{A}\tilde{U}^2}\int_0^{1+\frac{\Xi}{R}\tilde{\eta}} \tilde{v}_z^2 \tilde{r} d\tilde{r}$ is a coefficient depending on the axial velocity profile $\tilde{v}_z(\tilde{r},\tilde{z},\tilde{t})$. This system is not closed since the coefficient $\tilde{\alpha}$ and the wall shear stress term $[\frac{\partial \tilde{v}_z}{\partial \tilde{r}}]_{\tilde{\Sigma}}$ depend on the axial velocity profile which needs to be prescribed. To obtain a closed, well-defined problem which can be solved numerically, an assumption on the form of the axial velocity profile, *i.e.* an *ad hoc* closure, needs to be used. Typical axial velocity profile used in the literature is the following polynomial relationship between $\tilde{v}_z$ and $\tilde{r}$:

$$\tilde{v}_z(\tilde{r},\tilde{z},\tilde{t}) = \frac{\gamma+2}{\gamma}\tilde{U}(\tilde{z},\tilde{t}) \left(1 - \left(\frac{\tilde{r}}{1 + \frac{\Xi}{R}\tilde{\eta}(\tilde{z},\tilde{t})}\right)^\gamma\right). \tag{3.21}$$

Here exponent $\gamma = 2$ corresponds to the Poiseuille velocity profile and $\gamma = 9$ approximates an "almost flat" velocity profile.[23] Other suggestions include a flat velocity profile with a small linear boundary layer (Bingham flow).[20] Using the closure (3.21) gives a one-dimensional system, which reads (in dimensional variables):

$$\frac{\partial A}{\partial t} + \frac{\partial m}{\partial z} = 0, \tag{3.22}$$

$$\frac{\partial m}{\partial t} + \frac{\partial}{\partial z}\left(\alpha\frac{m^2}{A}\right) + \frac{A}{\rho_{\text{F}}}\frac{\partial p}{\partial z} = -\frac{2\mu}{\rho_{\text{F}}}(\gamma+2)\frac{m}{A}. \tag{3.23}$$

For $\gamma = 9$ one gets $\alpha = 1.1$. Here $A = (R+\eta)^2$ and $m = AU$, where U is the cross-sectional average of the axial fluid velocity.

To completely specify the problem, the pressure needs to be given in terms of the unknown functions A and/or m. This describes the wall behavior. A typical choice in literature is the Law of Laplace

$$p = p_{\text{ref}} + \frac{Eh}{(1-\sigma^2)R}\left(\sqrt{\frac{A}{A_0}} - 1\right) \tag{3.24}$$

where $A_0 = R^2$ is the reference cross-sectional area. This is Eq. (3.18) assuming zero stress at reference configuration. The resulting system is a hyperbolic system

of partial differential equations for the unknown functions A and m.

The viscoelastic model (3.13) with $C_v \neq 0$, can be used to model the viscoelastic wall behavior using the one-dimensional model (3.22), (3.23). Equation (3.13) written in terms of the cross-sectional area, in dimensional variables, reads

$$p = p_{\text{ref}} + \left(\frac{Eh}{(1-\sigma^2)R} + p_{\text{ref}}\right)\left(\sqrt{\frac{A}{A_0}} - 1\right) + \frac{hC_v}{R}\frac{\partial}{\partial t}\left(\sqrt{\frac{A}{A_0}}\right). \tag{3.25}$$

Drawbacks of the One-Dimensional Model

Notice again that the assumption on the velocity profile directly influences the wall-shear stress term. Thus, the wall-shear stress predicted by this model will incorporate the error made by an *ad hoc* velocity profile assumption. Figure 3 illustrates a discrepancy between the axial velocity profiles obtained using the one-dimensional model with an *ad hoc* closure (3.21) for $\gamma = 9$ and the Womersley profile obtained using the reduced model discussed in the next section.

Another drawback of the one-dimensional model is related to the fact that viscous effects in this model are described in terms of the viscous drag force $-\frac{2\mu}{\rho_F}(\gamma+2)\frac{m}{A}$ and not in terms of the viscous dissipation described by the second-order derivatives in the original equations. As a result, system (3.22), (3.23) is hyperbolic, unlike the original Navier–Stokes system. This means, in particular, that this model predominantly captures propagation of waves in the vessel wall, whereas the fluid viscosity enters only as a sink in the balance of axial momentum. The study of wave propagation on finite (bounded) domains using "wave-like" equations such as (3.22), (3.23), typically leads to boundary wave reflections. This is particularly the case when measured pressure or flow rate data are used as the boundary data. This data incorporates information from the actual problem that is not being "recognized" or "processed" by the oversimplified one-dimensional model. In turn, the model produces reflected waves that are not present in the actual problem. Figure 4 shows the reflected waves superimposed over the main wave front obtained as a solution of the 1D hyperbolic model using the two-step Lax–Wendroff method, previously tested in Ref.[7] The simulation presented in Fig. 4 was obtained for the spatial grid size of $dx = 0.0028$ and time step $dt = 1.3418 \times 10^{-}4$, corresponding to the CFL number of 0.5. We varied the CFL number and the spatial grid size to test the stability and convergence of the method. The maximum norm of

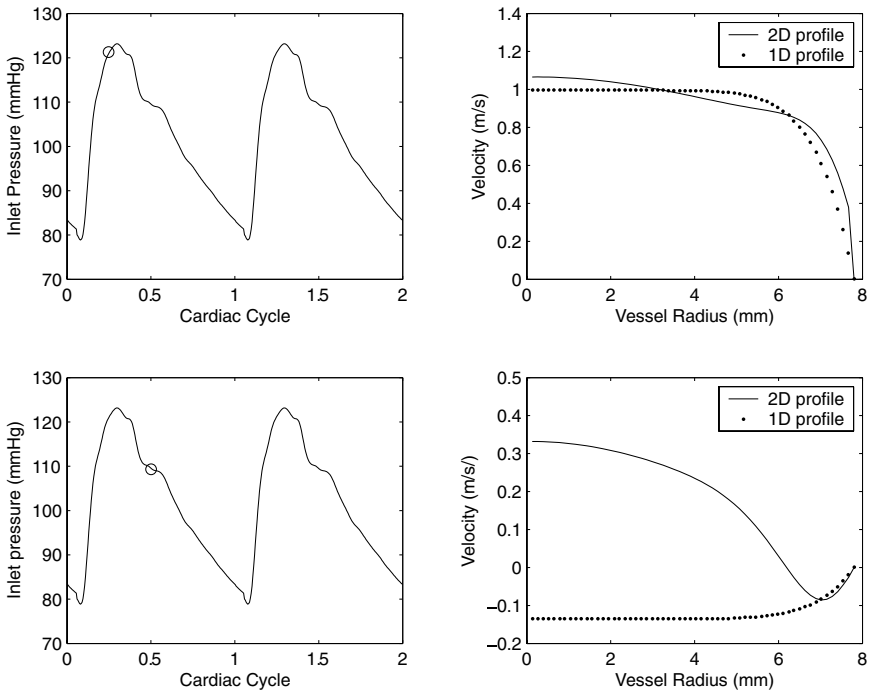

FIGURE 3. Comparison of the axial velocity profiles between the one-dimensional and the one-and-a-half-dimensional model presented in the section on "The One-and-a-Half-Dimensional Reduced Model" at two different times in the cardiac cycle. The values of the nondimensional parameters defined in (3.17) are *Sh* = 26 and *Re* = 1200.

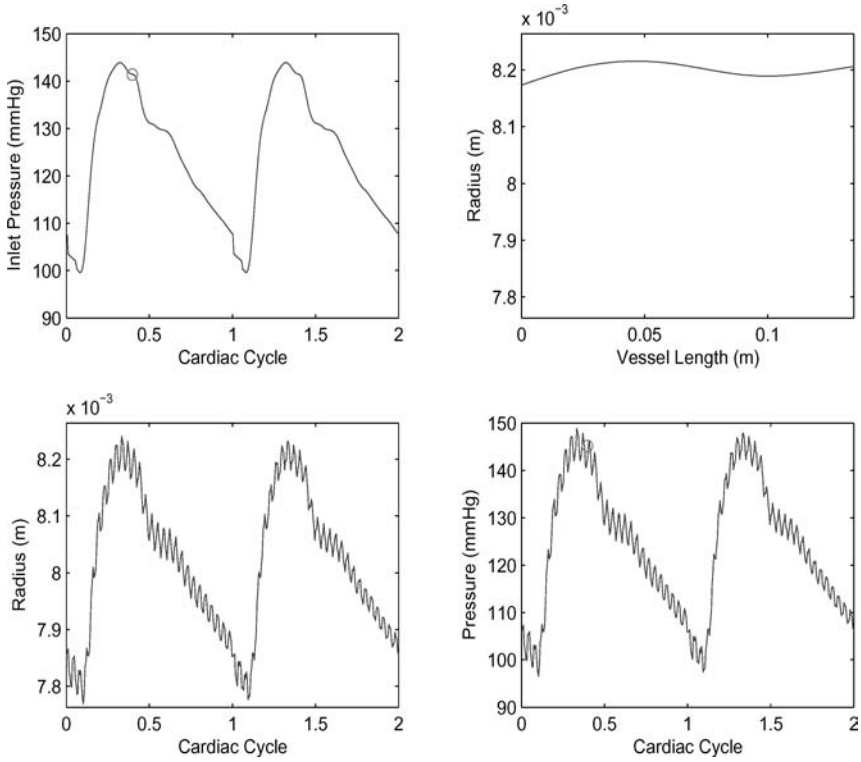

FIGURE 4. Numerical solution of the one-dimensional model showing high-frequency, short wave-length reflected waves superimposed over the main wave front ($R = 0.0078$ m, $L = 0.135$ m, $E = 674700$ Pa, $h = 0.001$ m).

the difference in the displacement between two different runs was used as an indicator of convergence. The results presented in Fig. 4 showed less than 3% difference between the results of the simulation with half the spatial grid size $dx = 0.0014$, and the time step $dt = 3.5 \times 10^{-5}$, corresponding to the CFL number of 0.25. We concluded that the high frequency oscillations shown in Fig. 4 were not a consequence of the numerical solver.

The present paper considers an effective model that gets around both drawbacks. The model equations are *closed*, namely, the axial velocity profile follows from the original equations themselves and is not prescribed *a priori*, and the viscous dissipation due to the viscosity of the fluid is kept, to the leading order. We show in the section on "Visoelasticity of the Fluid-Structure Interaction" that this resolves the inlet and outlet boundary reflections produced by the one-dimensional model.

The One-and-a-Half-Dimensional Reduced Model

The reduced model studied in this work is obtained from the two-dimensional equations presented in the section on "The Two-Dimensional Reduced Equations" using further asymptotic analysis and homogenization theory. The details of the calculation are similar to those presented in Ref.[9] The resulting model is two-dimensional, but it has a special form which allows the use of one-dimensional numerical techniques for the numerical calculation of the solutions. Taking this reduced complexity of the resulting model into account, we refer to it as a one-and-a-half-dimensional reduced model. The reduced equations hold under the following assumptions:

- (1) The domain is cylindrical with small aspect ratio $\varepsilon = R_{\max}/L$
- (2) Longitudinal displacement is negligible.
- (3) Radial displacement is not too large, {i.e.}, $\delta := \Xi/R \leq \varepsilon$.
- (4) The reference tube radius varies slowly: $R'(z) \leq \epsilon$
- (5) The Reynolds number Re is small to medium ($Re \approx 800$).
- (6) The z-derivatives of the nondimensional quantities are $O(1)$ (not too large).

Introducing the following notation for the expansions of the unknown functions in dimensional variables

$$v_z = v_z^{0,0} + v_z^{0,1} + v^{1,0}, v_r = v_r^{1,0},$$
$$\eta = \eta^{0,0} + \eta^{0,1} + \eta^{1,0}, p = p^{0,0} + p^{0,1}.$$

The first superscript denotes the asymptotic expansion with respect to the aspect ratio ϵ and the second with respect the radial displacement $\delta = \Xi/R$. For example, $v_z = v_z^{0,0} + v_z^{0,1} + v^{1,0} = V(\tilde{v}_z^{0,0} + \delta\tilde{v}_z^{0,1} + \epsilon\tilde{v}_z^{1,0} + O(\epsilon^2))$, etc.

The reduced "one-and-a-half-dimensional" equations holding in cylindrical domains with slowly varying reference radius $R = R(z)$ then read:

The 0th order approximation: Find $(\eta^{0,0}, v_z^{0,0})$ such that

$$\frac{\partial \eta^{0,0}}{\partial t} + \frac{1}{R}\frac{\partial}{\partial z}\int_0^R r v_z^{0,0} dr = 0,$$

$$\varrho_F \frac{\partial v_z^{0,0}}{\partial t} - \mu \frac{1}{r}\frac{\partial}{\partial r}\left(r\frac{\partial v_z^{0,0}}{\partial r}\right) = -\frac{\partial p^{0,0}}{\partial z}, \qquad (3.26)$$

$$v_z^{0,0}|_{r=0} - \quad \text{bounded}, \quad v_z^{0,0}|_{t=R} = 0, \quad v_z^{0,0}|_{t=0} = 0,$$

$$\eta^{0,0}|_{t=0} = 0, \quad p^{0,0}|_{z=0} = P_0, \; p^{0,0}|_{z=L} = P_L \; ,$$

where

$$p^{0,0} = \left(\frac{Eh}{(1-\sigma^2)R} + p_{\text{ref}}\right)\frac{\eta^{0,0}}{R} + \frac{hC_v}{R^2}\frac{\partial \eta^{0,0}}{\partial t} \; . \quad (3.27)$$

The δ correction: Find $(\eta^{0,1}, v_z^{0,1})$ such that

$$\frac{\partial \eta^{0,1}}{\partial t} + \frac{1}{R}\frac{\partial}{\partial z}\int_0^R r v_z^{0,1} dr = -\frac{1}{2R}\frac{\partial}{\partial t}(\eta^{0,0})^2,$$

$$\varrho_F \frac{\partial v_z^{0,1}}{\partial t} - \mu \frac{1}{r}\frac{\partial}{\partial r}\left(r\frac{\partial v_z^{0,1}}{\partial r}\right) = -\frac{\partial p^{0,1}}{\partial z} \qquad (3.28)$$

$$v_z^{0,1}|_{r=0} - \quad \text{bounded}, \quad v_z^{0,1}|_{r=R} = -\eta^{0,0}\frac{\partial v_z^{0,0}}{\partial r}|_{r=R},$$

$$v_z^{0,1}|_{t=0} = 0, \, \eta^{0,1}|_{t=0} = 0, \quad \eta^{0,1}|_{z=0} = 0, \quad \eta^{0,1}|_{z=L} = 0 \; ,$$

where

$$p^{0,1} = \left(\frac{Eh}{(1-\sigma^2)R} + p_{\text{ref}}\right)\left(\frac{\eta^{0,1}}{R} - \left(\frac{\eta^{0,0}}{R}\right)^2\right)$$

$$+ \frac{hC_{\text{v}}}{R^2}\left(\frac{\partial \eta^{0,1}}{\partial t} - \frac{\eta^{0,0}}{R}\frac{\partial \eta^{0,1}}{\partial t}\right) \; . \qquad (3.29)$$

The ε correction: Find $(v_r^{1,0}, v_z^{1,0})$ such that

$$v_r^{1,0}(r,z,t) = \frac{1}{r}\left(R\frac{\partial \eta^{0,0}}{\partial t} + \int_r^R \xi \frac{\partial \eta_z^{0,0}}{\partial z}(\xi, z, t) d\xi\right), \quad (3.30)$$

$$\rho_{\text{F}}\frac{\partial v_z^{1,0}}{\partial t} - \mu\frac{1}{r}\frac{\partial}{\partial r}\left(r\frac{\partial v_z^{1,0}}{\partial r}\right)$$

$$= -\rho_{\text{F}}\left(v_r^{1,0}\frac{\partial v_z^{0,0}}{\partial r} + v_z^{0,0}\frac{\partial v_z^{0,0}}{\partial z}\right), \qquad (3.31)$$

$$v_z^{1,0}|_{\bar{r}=0} - \text{ bounded}, \quad v_z^{1,0}|_{r=R} = 0, \quad v_z^{1,0}|_{t=0} = 0.$$

Final solution:

$$v_z = v_z^{0,0} + v_z^{0,1} + v^{1,0}, v_r = v_r^{1,0},$$

$$\eta = \eta^{0,0} + \eta^{0,1} + \eta^{1,0}. \qquad (3.32)$$

For the elastic membrane model, namely for $C_{\text{v}} = 0$, it was proved in Ref. [9] that under assumptions (1)–(6), the functions (3.32) satisfying (3.26)–(3.31), solve the three-dimensional axially symmetric problem described in the section on "Description of the Problem to the ϵ^2-accuracy.

Remarks on the reduced model (3.26)–(3.31):

- The first equation in each of the three problems (3.26)–(3.31) all follow from the conservation of mass principle.
- The second equation in each of the three problems (3.26)–(3.31) correspond to the balance of momentum. The quadratic advection terms appear only in the ϵ-correction as the right-hand side of equation (3.31). In addition, they are linearized around the $(0,0)$-approximation and thus present no additional difficulty in the numerical simulation of the model.
- The original moving boundary problem, posed on the domain with a moving lateral boundary $\Sigma(t)$, has now been approximated by a series of three problems (3.26)–(3.31) each defined on a fixed domain with radius $R = R(z)$.

This model enabled us to study, among other things, wave propagation in arteries influenced by two distinct viscous effects. One is the influence of fluid viscosity and the other is the influence of vessel wall viscosity. We shall see below how they have different viscoelastic impact on the vessel wall dynamics. We first present the numerical algorithm for calculation of the solution of the model equations (3.26) and (3.28).

NUMERICAL ALGORITHM

To solve problems (3.26) and (3.28) numerically it is convenient to rewrite each of the systems of equations as a second-order hyperbolic-parabolic problem. Namely, after differentiating the first equation in (3.26) with respect to time, and plugging the second equation into the first, problem (3.26) can be rewritten as

$$\frac{\partial^2 \eta^{0,0}}{\partial t^2} - \frac{R}{2\rho F}\frac{\partial^2 p^{0,0}}{\partial z^2} = -\frac{\mu}{\rho F}\frac{\partial}{\partial z}\left(\frac{\partial v_z^{0,0}}{\partial r}|_{r=R}\right), \quad (4.33)$$

$$\rho_{\text{F}}\frac{\partial v_z^{0,0}}{\partial t} - \mu\frac{1}{r}\frac{\partial}{\partial r}\left(r\frac{\partial v_z^{0,0}}{\partial r}\right) = -\frac{\partial p^{0,0}}{\partial z} \; , \quad (4.34)$$

with the initial and boundary conditions specified in (3.26) where $p^{0,0}$ is substituted by (3.27). Similarly, problem (3.28) can be written as

$$\frac{\partial^2 \eta^{0,1}}{\partial t^2} - \frac{R}{2\rho_{\text{F}}}\frac{\partial^2 p^{0,1}}{\partial z^2} = -\frac{\mu}{\rho_{\text{F}}}\frac{\partial}{\partial z}\left(\frac{\partial v_z^{0,0}}{\partial r}|_{r=R}\right)$$

$$-\frac{1}{2R}\frac{\partial^2}{\partial t^2}(\eta^{0,0})^2, \qquad (4.35)$$

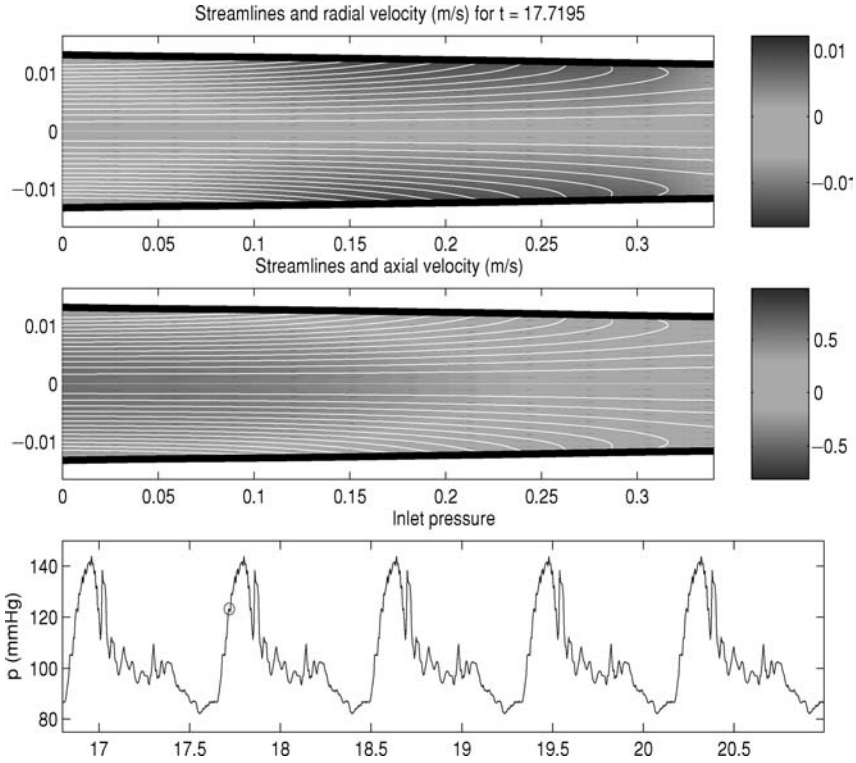

FIGURE 5. A snap-shot of the radial (*top*) and longitudinal (*middle picture*) component of the velocity with the superimposed streamlines, calculated at the beginning of the cardiac (LVAD) output. The *circle* at the bottom graph shows the time in the cardiac cycle when the snap-shot is taken.

$$\rho_{\mathrm{F}}\frac{\partial v_z^{0,1}}{\partial t}-\mu\frac{1}{r}\frac{\partial}{\partial r}\left(r\frac{\partial v_z^{0,1}}{\partial r}\right)=-\frac{\partial p^{0,1}}{\partial z}\,, \qquad (4.36)$$

with initial and boundary conditions given in (3.28), and $p^{0,1}$ substituted by (3.29).

The first equation in both subproblems can be thought off as a one-dimensional wave equation in z and t, and the second as the one-dimensional heat equation in r and t. The systems for the 0, 0 and 0, 1 approximations have the same form. They are solved using a 1D Finite Element Method. Since the mass and stiffness matrices are the same for both problems, up to the boundary conditions, they are generated only once. Both systems are solved simultaneously using a time-iteration procedure. First the parabolic equation is solved for $v_z^{0,0}$ at the time step t_{i+1} by explicitly evaluating the right-hand side at the time-step t_i. Then the wave equation is solved for $\eta^{0,0}$ with the evaluation of the right-hand side at the time-step t_{i+1}. Using these results for $v_z^{0,0}$ and $\eta^{0,0}$, computed at t_{i+1}, a correction at t_{i+1} is calculated by repeating the process with the updated values of the right-hand sides. This method is a version of the Douglas–Rachford time-splitting algorithm which is known to be of first-order accuracy.

Calculating approximation 1,0 is straightforward once the approximations 0, 0 and 0,1 are obtained.

In this algorithm a sequence of 1D problems is solved, so the numerical complexity is that of 1D solvers. However, leading order two-dimensional effects are captured to the ε^2-accuracy. Figures 5 and 6 show the axial and radial components of the velocity, together with the streamlines showing two-dimensional effects that cannot be captured using one-dimensional axially symmetric models.

We tested the numerical algorithm and the model Eqs. (3.26) and (3.28) by comparing our numerical results with the Womersley flow solution. Assuming fixed walls (high Young's modulus $E = 10^8$Pa) and sinusoidal pressure gradient, we calculated the solution of (3.26) and (3.28) numerically. The axial velocity profile is then compared to the exact solution corresponding to the Womersley flow. Figure 7 shows the comparison for a snap-shot in the sinusoidal cycle, obtained for the data $L = 0.1375$ m, $R = 0.004$ m, $p_0 - 0$, $p_L = 3500\sin(2\pi t/T)$ Pa. The Womersley profile appears to be identical to the numerically calculated profile resulting from Eqs. (3.26) and (3.28).

Finally, we compared the axial velocity profiles produced by the one-dimensional model (3.22), (3.23) with the axial velocity profile produced by the one-and-a-half dimensional model (3.26) and (3.28). For the one-dimensional model the *ad hoc* closure (3.21) with $\gamma = 9$ was used. The numerical solution was obtained using the two-step Lax–Wendroff method, previously tested in Ref.[7]

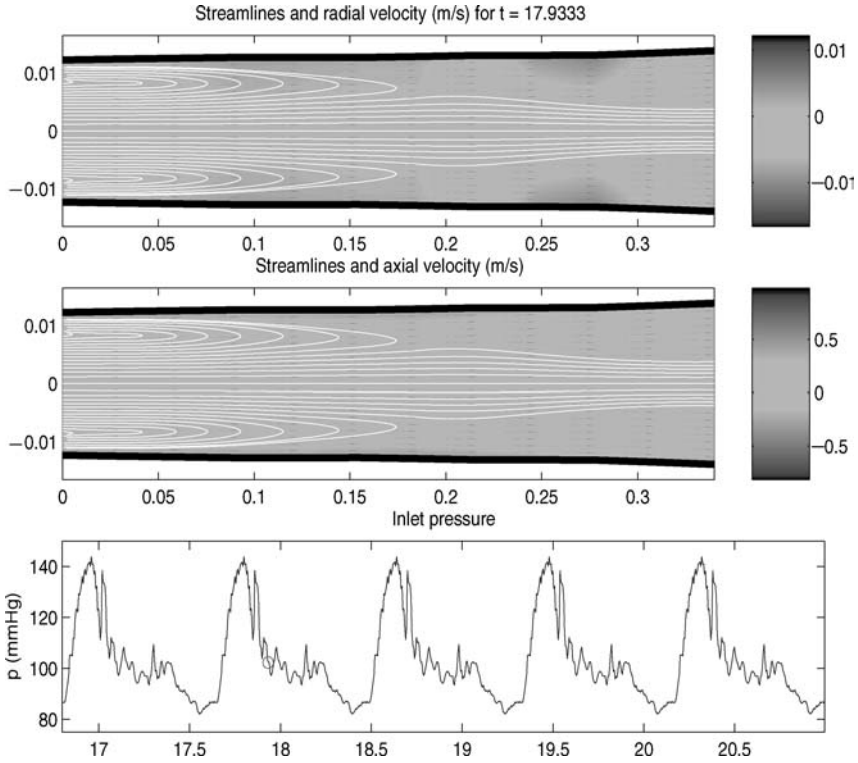

FIGURE 6. Same data as in Fig. 6 evaluated at a different time in the cardiac cycle.

The data used in this simulation were $R = 0.0078$ m, $L = 0.135$ m, $E = 674700$ Pa, $h = 0.001$ m. The values of the nondimensional parateters defined in (3.17) were $Sh = 26$ and $Re = 1200$. Figure 3 shows how the axial velocity profiles differ, indicating that the wall shear stress calculated using the one-dimensional models will incorporate the error made by the *ad hoc* assumption (3.21).

VISCOELASTICITY OF THE FLUID–STRUCTURE INTERACTION

Assume for the moment that the vessel walls are purely elastic, modeled by the linearly elastic membrane model, namely, by the model (3.13) with $C_v = 0$. Then, as we shall see below, the model described above shows that the dynamics of the linearly elastic walls caused by the motion of the viscous fluid exhibits viscoelastic behavior with the fluid imparting long-term memory effects on the motion of the elastic walls. More precisely, the following holds.

In Ref.[10], it was observed that (3.26) can be solved by considering the auxiliary problem

$$\frac{\partial \zeta}{\partial t} - \frac{1}{r}\frac{\partial}{\partial r}\left(r\frac{\partial \zeta}{\partial t}\right) = 0 \quad \text{in } (0, R) \times (0, \infty)$$

$$\zeta|_{r=0} \text{ is bounded}, \quad \zeta|_{R=0} = 0 \text{ and } \zeta|_{t=0} = 1,$$

and the mean of ζ in the radial direction $\mathcal{K}(t) = 2\int_0^R \zeta(r, t) r\, dr$, which can both be evaluated in terms of the Bessel's functions. The solution for the velocity $v_z^{0,0}$ (and also $v_z^{0,1}$) can then be written in terms of the convolution

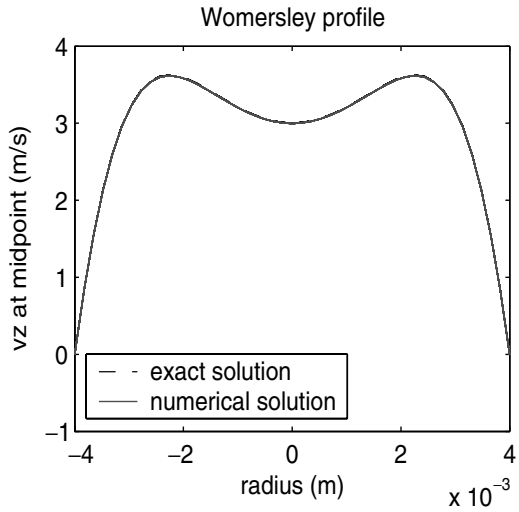

FIGURE 7. Womersley solution: A comparison between the exact Womersley solution and the numerical solution of (3.26) and (3.28) with rigid walls and sinusoidal pressure gradient. The two curves differ by less than 1%.

integral

$$\left(\mathcal{K}\star\frac{\partial\eta^{0,0}}{\partial z}\right)(z,t):=\int_0^t\mathcal{K}\left(\frac{\mu(t-\tau)}{\rho_F}\right)\frac{\partial\eta^{0,0}}{\partial z}(z,\tau)\,d\tau, \tag{5.37}$$

where $\mathcal{K}$ is the decreasing exponential function $exp(-\lambda\mu(t-\tau)/\rho_F)$ where λ is the first zero of the Bessel's function J_0. Now the problem for $\eta^{0,0}$ consists of solving the following initial-boundary value problem of "Biot type" with memory[5]:

$$\frac{\partial\eta^{0,0}}{\partial t}(z,t)=\frac{C}{2\rho_F R}\frac{\partial}{\partial z}\left(\mathcal{K}\star\frac{\partial\eta^{0,0}}{\partial z}\right)(z,t)\text{ on }(0,L)\times(0,+\infty) \tag{5.38}$$

$$\eta^{0,0}|_{z=0}=P_0/C,\quad \eta^{0,0}|_{z=L}=P_L/C$$

and

$$\eta^{0,0}|_{t=0}=0,$$

where $C=Eh/[(1-\sigma^2)R^2]+p_{\text{ref}}/R$.

The time integral in the convolution term uncovers the viscoelastic nature of the coupling between the motion of an elastic structure and a viscous fluid, explicitly. The viscous contribution of the fluid to the wave propagation in the elastic structure has a long-term memory effect. Due to the exponentially decaying kernel $\mathcal{K}$, history that happened long time ago affects the solution at the current time much less than the most recent history. To get a better feeling for the wave propagation described by Eq. (5.38), differentiate (5.38) with respect to time to obtain

$$\frac{\partial^2\eta^{0,0}}{\partial t^2}=C_1\frac{\partial^2\eta^{0,0}}{\partial z^2}-\frac{\mu}{\rho_F}C_2\frac{\partial}{\partial z}\left(\mathcal{K}'\star\frac{\partial\eta^{0,0}}{\partial z}\right). \tag{5.39}$$

Here C_1 and C_2 are constants that do not involve the viscosity coefficient μ. Thus, if $\mu=0$, the radial displacement η satisfies a constant-coefficient wave equation which describes propagation of waves in an elastic string. With $\mu\neq 0$, Eq. (5.39) describes wave propagation in a *viscoelastic string with long-term memory*.

The numerical method described in the section on "Numerical Algorithm," was used to obtain a solution of Eq. (5.39) with $\mu\neq 0$. Figure 8 shows the solution with $\mu=3.5\times10^{-3}$ kg/m/s. The solution contains only the main wave front, without the reflected waves appearing in one-dimensional models with Dirichlet boundary data, shown in Fig. 4. A direct comparison between the two solutions, one obtained by solving the one-dimensional system and the other by solving the one-and-a-half dimensional systems, is shown in Fig. 9. The data used in both simulations were $R=0.0078$ m, $L=0.135$ m, $E=674700$ Pa, $h=0.001$ m.

It is interesting to mention that the viscoelastic effect discussed in this section does not contribute to the hysteresis in the pressure-diameter diagram, typically observed in the vessel wall dynamics experimental measurements, see Refs.[1,4] The hysteresis behavior is solely due to the viscoelastic nature of the mechanical properties of vessel walls.

VISCOELASTICITY OF VESSEL WALLS

Determining the viscoelastic behavior of vessel walls is a complex problem. In Ref.[1], measurements of the viscoelastic aortic properties in dogs, and the derivation of the constitutive relation for the aortic wall behavior were obtained. In particular, the magnitude of the viscous modulus, corresponding to our coefficient hC_v/R is measured. The values corresponding to dogs aortas, reported in Ref.[1]. belong to the interval

$$\frac{hC_v}{R}|_{(\text{dog aorta})}\in(3.8\pm1.3\times10^4,7.8\pm1.1\times10^4)\ \text{dyn}\cdot\text{s/cm}^2$$
$$=(3.8\pm1.3\times10^3,7.8\pm1.1\times10^3)\,\text{Pa}\cdot\text{s}.$$

Taking into account the radius of the studied aortas ($\approx$ 0.008 m) and the average wall thickness ($\approx$ 0.0014 m), one obtains

$$C_v|_{(\text{dog aorta})}\in(2.17\times10^4,4.45\times10^4)\,\text{Pa}\cdot\text{s} \tag{6.39}$$

This coefficient appears to be slightly higher than the coefficient C_v describing the wall properties of the human femoral and carotid arteries, although their viscous moduli hC_v/R appear to be of the same order of magnitude. Namely, measurements reported in Ref.[2] imply that in healthy humans the magnitude of the coefficient multiplying the term $\partial D/\partial t$. where D is the vessel diameter, is estimated to be equal to 266×Pa·s/m. Using the values for the measured femoral artery diameter (0.00625 m) and the wall thickness (0.001 m), one obtains

$$C_v|_{(\text{human femoral})}\approx5.2\times10^3\,\text{Pa}\cdot\text{s}. \tag{6.40}$$

Thus, the corresponding viscous modulus hC_v/R is

$$\frac{hC_v}{R}|_{(\text{human femoral})}\approx1.6\times10^3\,\text{Pa}\cdot\text{s}, \tag{6.41}$$

which is of the same order of magnitude as the viscous modulus corresponding to the dogs aortas.

In the present work these measurements were used as a guide in determining the order of magnitude of the coefficient hC_v/R that appears in the "effective" pressure–displacement relationship (3.13), which in dimensional variables reads

$$p-p_{\text{ref}}=\left(\frac{Eh}{(1-\sigma^2)R}+p_{\text{ref}}\right)\frac{\eta}{R}+\frac{hC_v}{R_2}\frac{\partial\eta}{\partial t}. \tag{6.42}$$

Using this constitutive model for the vessel wall behavior, coupled with the reduced equations (3.26)–(3.31), numerical simulations with the data given in Table 1 were obtained. Figure 10 (right) shows the results of the numerical simulations for the inlet and outlet pressure data shown in Fig. 11

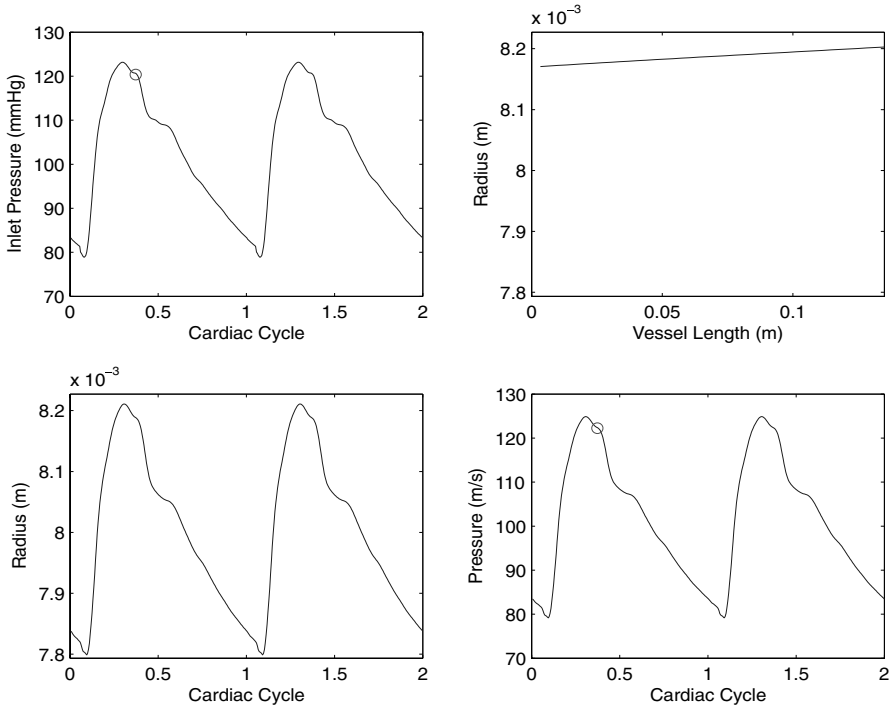

FIGURE 8. Numerical solution of the one-and-a-half-dimensional reduced model including viscous dissipation.

(left). The top figure on the right shows the pressure and the scaled diameter in one cardiac cycle. Both waves exhibit the same morphology, but the diameter shows a time delay with respect to the pressure, which is due to the viscosity of the vessel wall. The bottom figure on the right shows the hysteresis behavior in the stress–strain relationship, where

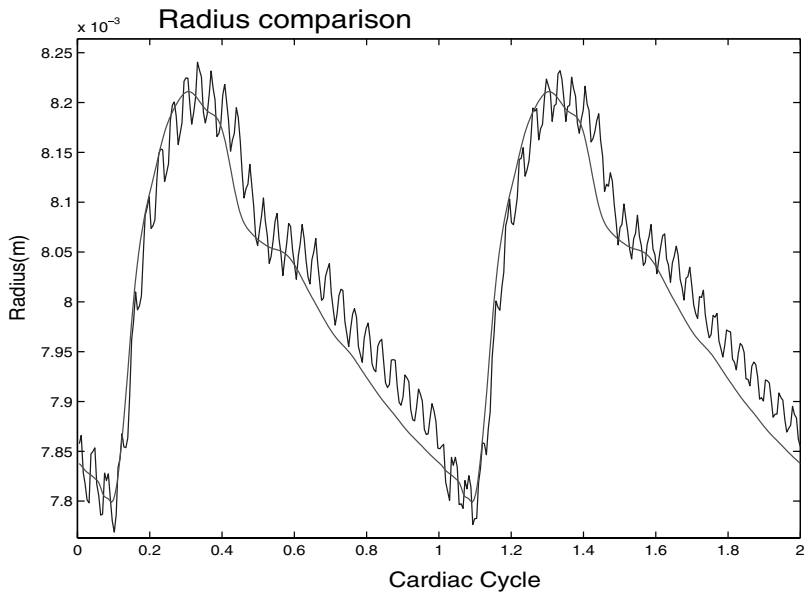

FIGURE 9. A comparison between two vessel radii at the midpoint of the tube in two cardiac cycles. The oscillatory graph corresponds to the solution of the one-dimensional model without the viscous fluid dissipation. The smooth graph corresponds to the solution of the reduced one-and-a-half dimensional model which includes viscous dissipation.

TABLE 1. Table with parameter values.

Parameters	Aorta/Iliacs	Latex tube
Char. radius R(m)	0.006–0.012	0.011
Char. length L(m)	0.065–0.2	0.34
Dyn. viscosity μ (kg/ms)	3.5×10^{-3}	3.5×10^{-3}
Young's modulus E(Pa)	10^5-10^6	1.0587×10^6
Wall thickness h(m)	$1-2\times10^{-3}$	0.0009
Wall density ρ_w (kg/m^2)	1.1	1.1
Fluid density ρ_F (kg/m^3)	1050	1000
Wall viscosity coef. hC_v/R(Pa·s)	$10^3-8\times10^3$	0

the stress (τ) and strain (e) are defined as in Ref. [1] using

$$\tau = \frac{2p(r_e r_i)^2}{r_e^2 - r_i^2}\frac{1}{R^2},\ \mathrm{e} = \frac{R+\eta}{R}, \qquad (6.43)$$

where r_e and r_i are the external and internal vessel radii calculated using $r_{e,i} = R \pm 0.5$ h. Each dot corresponds to one time step in one cardiac cycle. These graphs are compared with the measurements of the canine aorta (two graphs on the left), reported in Ref.[1]. They show similar qualitative behavior.

Figure 12 shows another comparison between our numerical simulations and measurements. There, a pressure–diameter relationship is plotted, showing hysteresis behavior. The graph in Fig. 12 (left) corresponds to the measurements of the human femoral artery reported in Ref.[2], and the graph in Fig. 12 (right) shows the pressure–diameter relationship in the simulations obtained using the reduced one-and-a-half dimensional model, for the parameters shown in Table 1. Again, similar viscoelastic behavior is detected.

It is worth mentioning that it was impossible to recreate the numerical simulations corresponding to the same set of data as those used in the measurements reported in Refs.[1,2] due to the insufficient information about the inlet and outlet pressure data of the tested experimental segment.

EXPERIMENTAL VALIDATION

A mock circulatory loop was utilized to validate the one-and-a-half-dimensional fluid–structure interaction model, presented in the section on "The One-and-a-Half-Dimensional Reduced Model." The flow loop consists of a Left Ventricular Assist Device (LVAD HeartMate, Thoratex Corp., Woburn, MA) serving as a pulsatile flow pump, inlet and outlet valves, latex tubing (Kent Elastomer Products Inc.) serving as the compliant flow conduit, a Nalgene canister as the reservoir, and two compliance chambers (wash bottles; 250 ml in volume). This is similar to the design of the flow loop described in Ref.[22] except for the tubing which is compliant in this case. A sketch of the flow loop is shown in Fig. 13. The test segment of the compliant tube was 34 cm long. At the inlet and outlet of the test segment, pressure

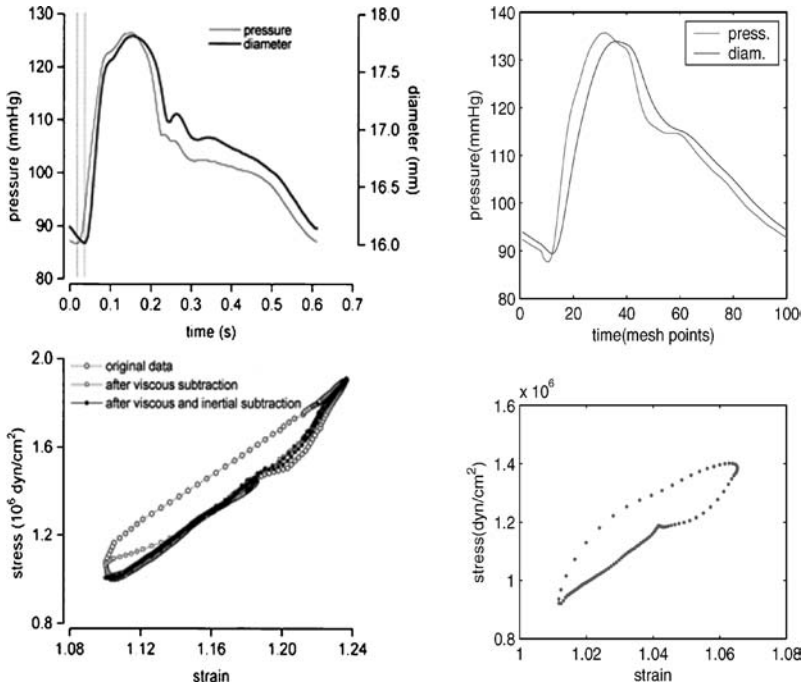

FIGURE 10. ***Left*: Measured viscoelastic behavior of the canine aorta reported in Ref.[1] (*top*: aortic diameter and pressure wave forms, *bottom*: stress–strain relationship). *Right*: Numerical simulation of the reduced one-and-a-half dimensional model showing viscoelastic behavior of vessel walls (*top*: aortic diameter and pressure wave forms, *bottom*: stress–strain relationship).**

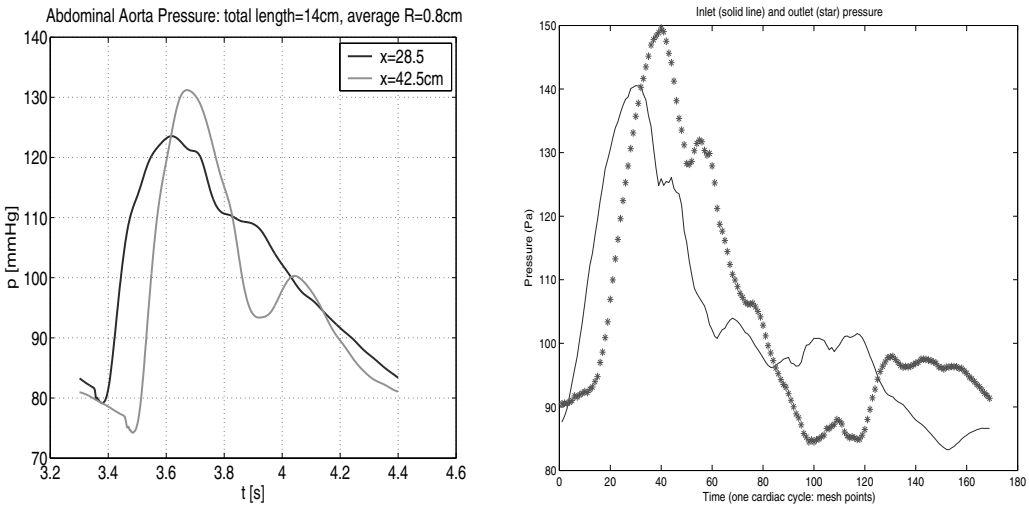

FIGURE 11. Inlet and outlet pressure data used in the numerical simulations. *Left*: aortic data[12]; *Right*: Circulatory flow loop data (filtered).

transducers (TruWave. Edwards Lifesciences, Irvine, CA) measured the systolic/diastolic pressure of 148/84 mmHg. The pressure waves were recorded during 25 cardiac cycles. The graphs in Fig. 11 (right) show the inlet and outlet (filtered) pressure data over one cardiac cycle.

The diameter of the tube was measured at the reference pressure of 84 mmHg to be $d = 2.22$ cm with the wall thickness of $h = 0.09$ cm. The Young's modulus of the tube wall was obtained by comparing the diameters of the tube at the reference pressure and at the maximal pressure of 148 mmHg where $d = 2.38$ cm, utilizing the linear pressure–displacement relationship (3.18). The maximal measured radial displacement equals 0.8 mm which is in excellent agreement with the numerically calculated displacement shown in Fig. 14.

Ultrasonic imaging and Doppler methods were used to measure axial velocity of the flow. Nondairy coffee creamer was dispersed in water to enable reflection for ultrasound measurements. A high-frequency (20 MHz) Doppler probe custom built in our laboratory was inserted through a flexible catheter introducer located at the distal end of the flow section and connected to a pulsed Doppler velocimeter also constructed in our laboratory. The probe consisted of a 1.0 mm diameter Doppler crystal focused at 4 mm and mounted at the tip of a 30 cm long by 2 mm diameter stainless steel tube. The probe was long enough to be positioned anywhere within the flow section with the sound beam oriented against the direction of flow to measure the axial component of fluid velocity. This method has been validated *in-vivo* by measuring the velocity and wall motion in mice to a precision of 0.1 μm, see Refs.[17,18]. Figure 15 shows a

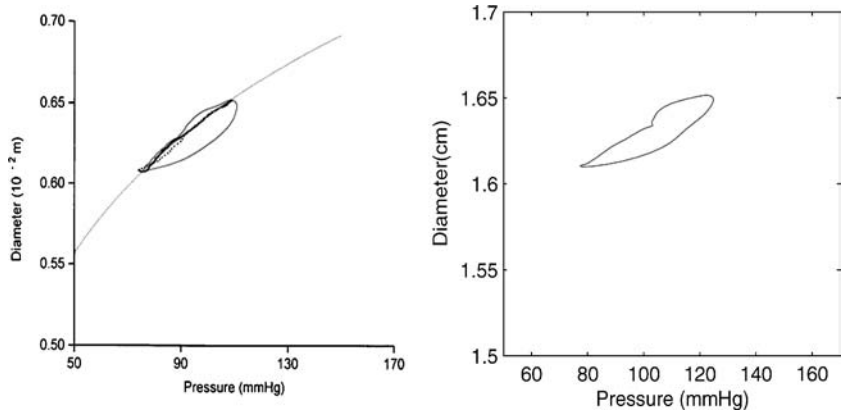

FIGURE 12. *Left*: Measurements of the diameter–pressure hysteresis loop in human femoral artery reported in Ref.[2]. *Right*: Numerical simulation of the diameter–pressure hysteresis loop with parameters from Table 1 ($E = 1.3 \times 10^6$ Pa, $h = 0.001$ m, $R = 0.008$ m, $L = 0.13$ m, $hC_{v/R} = 10^3$ Pa·s), and pressure data shown in Fig. 4.

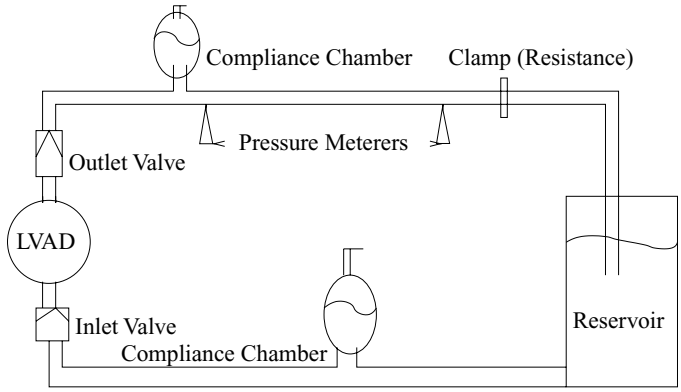

FIGURE 13. A sketch of the mock circulatory flow loop.

comparison between the experimentally measured and numerically calculated axial component of the velocity, evaluated at the midpoint of the tube (midpoint with respect to the length and the diameter of the tube). The latex tube walls were modeled using the linearly elastic membrane model. Less than 3% of difference in the velocity and less that 1% difference in the maximum diameter was detected, showing excellent agreement between the model and the experiment.

DISCUSSION

The reduced model studied in this work describes main features of blood flow in major compliant arteries. Compliant behavior of arterial walls was modeled by the linearly viscoelastic membrane equations. The resulting model holds in the axially-symmetric sections of the vascular system. The numerical simulations capturing the flow and wall dynamics are fast and simple, requiring only one-dimensional numerical techniques, while producing solutions that capture two-dimensional fluid flow effects to the ϵ^2-accuracy, where ϵ is the aspect ratio of the vessel section. Two-dimensional effects are evident in Figs. 5 and 6 where radial and longitudinal components of the velocity are depicted, together with the streamlines, at two different times in the cardiac cycle. Secondary flows, shown in these

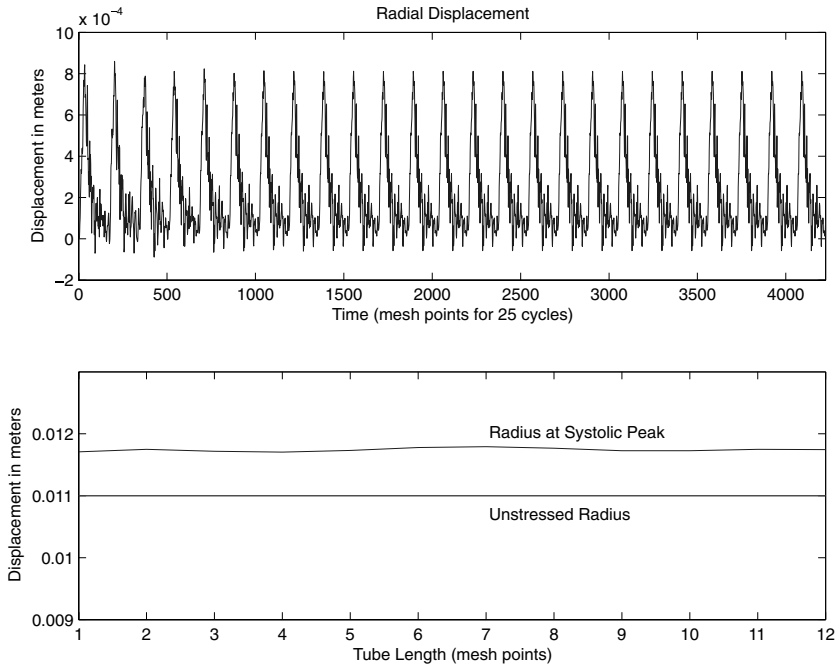

FIGURE 14. The graph on the *top* of the figure shows the numerically calculated radial displacement of the tube wall. The maximum displacement corresponds well to the measured maximum displacement of 8×10^{-4} m. The graph at the *bottom* of the figure shows the radius of the tube wall numerically calculated along the tube length at the systolic peak.

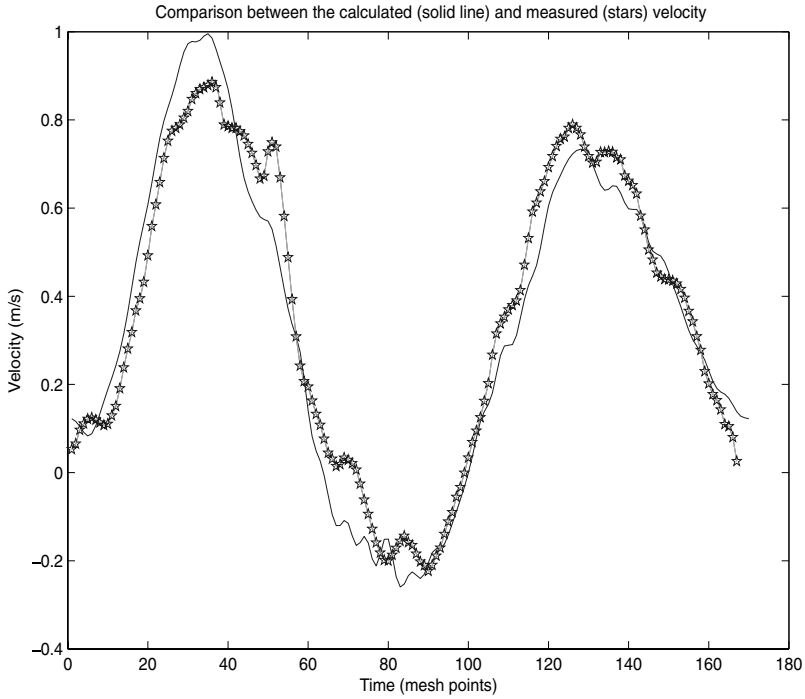

FIGURE 15. The figure shows a comparison between the experimentally measured and numerically calculated axial component of the velocity, evaluated at the midpoint of the tube (midpoint with respect to the length and the diameter of the tube).

figures, cannot be captured using one-dimensional axially symmetric models.

In addition to capturing the secondary flow effects, the model obtained in this work captures the explicit form of the viscoelastic behavior of the wall due to the coupled dynamics with the viscous fluid. This is described by Eq. (5.38). The convolution integral in Eq. (5.38) indicates that the displacement is affected by the viscosity of the fluid through a long-term memory effect. This viscoelastic term smooths out the high frequency oscillations due to the reflected waves in the displacement and pressure. However, the viscosity of the fluid does not affect the hysteresis in the pressure–diameter relationship. The hysteresis, typically detected in the measurements of the pressure–diameter relationship (and stress–strain relationship),[1,2] is solely due to the viscoelastic nature of the mechanical properties of vessel walls. In fact, it was shown in this work that the linearly viscoelastic thin shell (membrane) model coupled with the reduced flow equations, captures the main features of the arterial wall hysteresis. More precisely, a time-lag between the pressure and diameter waves, similar to those observed in the measurements in Ref.[1] was detected with the reduced model, and the hysteresis such as those obtained in experimental measurement of canine aorta[1] and healthy human femoral arteries[2] were recovered, see Figs. 10 and 12.

The model obtained in this work provides a sophysticated but simple and efficient description of blood flow in axially symmetric sections of the vascular system. It recovers information about blood flow and vessel wall dynamics that cannot be captured using standard one-dimensional models. This model predicts local hemodynamics and wall shear stress to the higher order accuracy and can thus be used as a better predictor of possible pathologies in the cardiovascular function. It's simple form makes this model particularly suitable for the use in multiscale simulations when larger sections of the cardiovascular system are simulated using a cascade of models of different dimension.

Various generalizations of this model are under way. They include modifications of the model to capture stiffening of vessel walls and presence of endovascular prostheses like stents or stent-grafts. Further developments include the implementation of the conditions that hold at vascular bifurcations so that the model presented in this work can be used to study blood flow, for example, in bifurcated prostheses such as those used in endovascular treatment of aortic abdominal aneurysm. When completed, this method will provide an efficient way to study, for example, improved design of bifurcated prostheses to minimize complications such as graft limb thrombosis associated with high temporal shear stress gradients reported for certain endografts.

ACKNOWLEDGMENTS

Research of Čanić, Hartley, Rosenstrauch, Tambača and Mikelić is supported in part by the joint National Sci-

ence Foundation and the National Institutes of Health grant DMS-0443826. In addition, research of Čanić is supported in part by the National Science Foundation under grants DMS-0245513, DMS-0337355, and the research of Hartley is supported in part by the National Institutes of Health under Grant HL22512. The experimental design and the *in vitro* work at Dr. Rosenstrauch's laboratory at the Texas Heart Institute was partially supported by a grant from the Roderick Duncan McDonald Foundation at the St. Luke's Episcopal Hospital. Kent Elastomer Inc. donation of latex tubing is also acknowledged. The authors would like to thank undergraduate student Joy Chavez for the help with data collection and flow loop experiments. Chavez's research was supported by the NSF under grant DMS-0337355.

REFERENCES

[1]Armentano, R. L., J. G. Barra, J. Levenson, A. Simon, and R. H. Pichel. Arterial wall mechanics in conscious dogs: Assessment of viscous, iner-tial, and elastic moduli to characterize aortic wall behavior. *Circ. Res.* 76:468–478, 1995.

[2]Armentano, R. L., J. L. Megnien, A. Simon, F. Bellenfant, J. G. Barra, and J. Levenson. Effects of hypertension on viscoelasticity of carotid and femoral arteries in humans. *Hypertension* 26:48–54, 1995.

[3]Barnard, A. C. L, W. A. Hunt, W. P. Timlake, and E. Varley. A theory of fluid flow in compliant tubes. *Biophys. J.* 6:717–724, 1966.

[4]Bauer R. D., R. Busse, A. Shabert, Y. Summa, and E. Wetterer. Separate determination of the pulsatile elastic and viscous forces developed in the arterial wall *in vivo*. *Pflugers Arch.* 380:221–226, 1979.

[5]Biot, M. A. Theory of propagation of elastic waves in a fluid-saturated porous solid. I. Lower frequency range, and II. Higher frequency range. *J. Acoust. Soc. Am.* 28(2):168–178, 179–191, 1956.

[6]Čanić, S., J. Tambača, G. Guidoboni, A. Mikelić, C. J. Hartley, and D. Rosenstrauch. Modeling viscoelastic behavior of arterial walls and their interaction with pulsatile blood flow. Submitted.

[7]Čanić, S., and E. H. Kim. Mathematical analysis of the quasilinear effects in a hyperbolic model of blood flow through compliant axisym-metric vessels. *Math. Methods Appl. Sci.* 26(14):1161–1186, 2003.

[8]Čanić, S., and A. Mikelić. Effective equations modeling the flow of a viscous incompressible fluid through a long elastic tube arising in the study of blood flow through small arteries. *SIAM J. Appl. Dyn. Sys.* 2(3):431–463, 2003.

[9]Čanić, S., A. Mikelić, D. Lamponi, and J. Tambača. Self-consistent effective equations modeling blood flow in medium-to-large compliant arteries. *SIAM J. Multisc. Anal. Simul.* 3(3):559–596, 2005.

[10]Čanić, S., A. Mikelić, and J. Tambača. A two-dimensional effective model describing fluid–structure interaction in blood flow: Analysis, simulation and experimental validation. Comptes Rendus Mech. Acad. Sci. Paris 333:867–883, 2005.

[11]Čanić, S., J. Tambača, A. Mikelić, C. J. Hartley, D. Mirković, and D. Rosenstrauch. Blood flow through axially symmetric sections of compliant vessels: New effective closed models. In: Proceedings of the 26th Annual International Conference. *IEEE Eng. Med. Bio. Soc.*, 2004, 10–13 pp.

[12]Chmielewski, C. Master of Science Thesis, Department of Mathematics, North Carolina State University, 2003.

[13]Eringen, A. Cemal. Mechanics of continua. New York: Wiley, 1967, 365 pp.

[14]Formaggia, L., D. Lamponi, and A. Quarteroni. One-dimensional models for blood flow in arteries. *J. Eng. Math.* 47:251–276, 2003.

[15]Formaggia, L., F. Nobile, and A. Quarteroni. A one-dimensional model for blood flow: Application to vascular prosthesis. In: Mathematical Modeling and Numerical Simulation in Continuum Mechanics, edited by Babuska, Miyoshi, and Ciarlet), Lect. Notes Comput. Sci. Eng. 19:137–153, 2002.

[16]Haidekker, M. A., C. R. White, and J. A. Frangos. Analysis of temporal shear stress gradients during the onset phase of flow over a backward-facing step. *J. Biomech. Eng.* 123:455–463, 2001.

[17]Hartley, C. J. Ultrasonic blood flow and velocimetry. In: McDonald's Blood Flow in Arteries, Theoretical, Experimental and Clinical Principles, 4th edn. Ch. 7, edited by W. W. Nichols and M. F. O'Rourke. London: Arnold, 1998, pp. 154–169.

[18]Hartley, C. J. G. Taffet, A. Reddy, M. Entman, and L. Michael. Noninvasive cardiovascular phenotyping in mice. *ILAR J.* 43:147–158, 2002.

[19]Nichols, W. W., and M. F. O'Rourke. McDonald's Blood Flow in Arteries: Theoretical, Experimental and Clinical Principles, 4th edn. New York: Arnold and Oxford University Press, 2000.

[20]Olufsen, M. S., C. S. Peskin, W. Y. Kim, E.M. Pedersen, A. Nadim, and J. Larsen. Numerical simulation and experimental validation of blood flow in arteries with structured-tree outflow conditions. *Ann. Biomed. Eng.* 28:1281–1299, 2000.

[21]Pontrelli, G. Modeling the fluid–wall interaction in a blood vessel. *Prog. Biomed. Res.* 6(4):330–338, 2001.

[22]Scott-Burden, T., J. P. Bosley, D. Rosenstrauch, K. Henderson, F. Clubb, H. Eichstaedt, K. Eya, I. Gregoric, T. Myers, B. Radovancevic, and O. H. Frazier. Use of autologous auricular chondrocytes for lining artificial surfaces: A feasibility study. *Ann. Thor. Surg.* 73(5):1528–1533, 2002.

[23]Smith, N. P., A. J. Pullan, and P. J. Hunter. An anatomically based model of transient coronary blood flow in the heart. *SIAM J. Appl. Math.* 62(3):990–1018, 2002.

[24]Tambača, J., S. Čanić, and A. Mikelić. Effective model of the fluid flow through elastic tube with variable radius. *Grazer Math. Ber.*, ISSN1016 7692 Bericht Nr. 3:1–22, 2005.